Crystal structure of the bacterial conjugation repressor FinO

Alexandru F. Ghetu[1], Michael J. Gubbins[2], Laura S. Frost[2] and J. N. Mark Glover[1]

[1]Department of Biochemistry, University of Alberta, Edmonton, Alberta, T6G 2H7, Canada. [2]Department of Biological Sciences, University of Alberta, Edmonton, Alberta, T6G 2E9, Canada.

The conjugative transfer of F-like plasmids is repressed by FinO, an RNA binding protein. FinO interacts with the F-plasmid encoded *traJ* mRNA and its antisense RNA, FinP, stabilizing FinP against endonucleolytic degradation and facilitating sense–antisense RNA recognition. Here we present the 2.0 Å resolution X-ray crystal structure of FinO, lacking its flexible N-terminal extension. FinO adopts a novel, elongated, largely helical conformation. An N-terminal region, previously shown to contact RNA, forms a positively charged α-helix (helix 1) that protrudes 45 Å from the central core of FinO. A C-terminal region of FinO that is implicated in RNA interactions also extends out from the central body of the protein, adopting a helical conformation and packing against the base of the N-terminal helix. A highly positively charged patch on the surface of the FinO core may present another RNA binding surface. The results of an *in vitro* RNA duplexing assay demonstrate that the flexible N-terminal region of FinO plays a key role in FinP–*traJ* RNA recognition, and supports our proposal that this region and the N-terminus of helix 1 interact with and stabilize paired, complementary RNA loops in a kissing complex.

The 35 kb transfer (*tra*) operon of the F-plasmid encodes the proteins responsible for conjugative transfer of this plasmid from host to recipient *Escherichia coli* cells[1]. Expression of the *tra* operon is repressed by the two component FinOP system that includes the 186 residue, basic protein FinO, and the ~79 nucleotide RNA, FinP[2]. FinP contains two stem-loop structures (SLI and SLII) and is complementary to the untranslated leader of *traJ*, which encodes the primary transcriptional activator of the *tra* operon[3]. FinP is thought to interact with *traJ* mRNA to occlude its ribosome binding site, blocking *traJ* translation and thereby inhibiting transcription of the *tra* operon[4].

Unprotected FinP is rapidly degraded by the cellular endonuclease RNase E and is, therefore, ineffective in repressing *traJ* translation[5]. FinO, the second component of the inhibition system, protects FinP against degradation. It binds to FinP and sterically blocks access to the RNase E cleavage site[5]. FinO also binds to the complementary stem-loop structures in *traJ* mRNA and promotes duplex formation between FinP and *traJ* RNA *in vitro*[6–8].

We showed that amino acids 26–61 and the remaining C-terminal residues (62–186) of FinO constitute two independent RNA binding regions[9]. The C-terminal region is also important for conferring RNase E resistance to FinP[10]. Within this region, residues 62–174 comprise a proteolytically stable domain that requires the rest of the C-terminal region (residues 175–186), or the N-terminal RNA binding region, for it to interact with RNA[9]. Here we present the crystal structure of a fragment of FinO (residues 26–186) that contains both RNA recognition regions. Using this structure, we have built a testable model of a complex of FinO bound to RNA comprising a minimal binding sequence and suggest a means by which FinO could facilitate FinP–*traJ* RNA interactions.

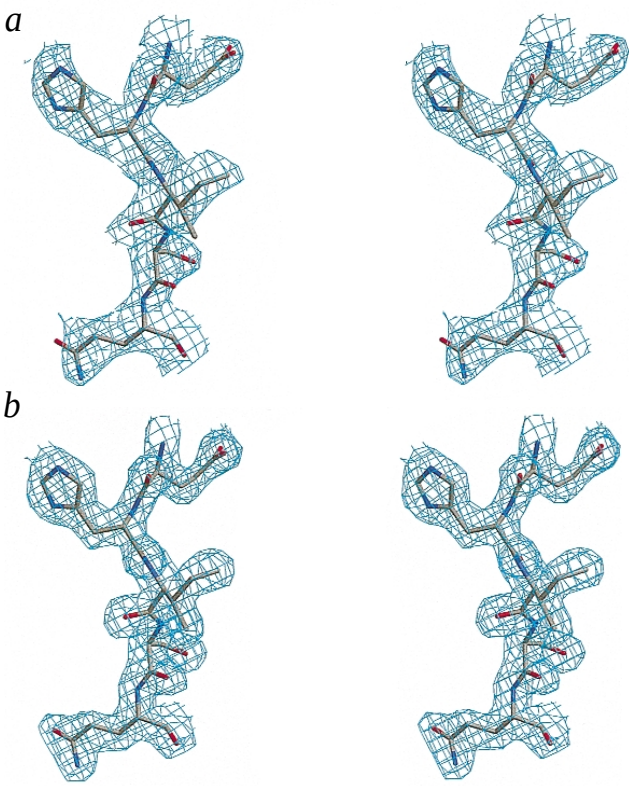

Fig. 1 Stereo view of electron density maps around residues 152–156 (on strand β4) with the final 2.0 Å refined model superimposed. ***a***, Density modified, 2.6 Å resolution MAD phased experimental map contoured at 1.0σ. ***b***, $2F_o - F_c$ map at 2.0 Å resolution using phases calculated from the final, refined model and contoured at 1.6σ.

Structure determination

FinO protein was overexpressed and purified from *E. coli* as described[9]. Attempts to crystallize full length FinO from the F-like plasmid R6-5 were unsuccessful. We have shown that FinO lacking only the N-terminal 25 amino acids (FinO(26–186)) comprises a proteolytically stable fragment at 4 °C that binds FinP RNA with the same affinity as the full length protein[9]. FinO(26–186) crystallized at 4 °C in the space group $P2_12_12_1$ (a = 37.57 Å, b = 38.73 Å, c = 145.42 Å) with one FinO molecule per asymmetric unit. The crystals diffracted X-rays weakly to 3.0 Å on a rotating anode X-ray source.

The structure of FinO(26–186) was solved by multiple wavelength anomalous dispersion (MAD) methods using selenomethionine substituted protein. Native FinO has only one methionine site at which selenomethionine can be introduced. To increase the phasing power of the data collected from selenomethionine substituted crystals, we mutated leucines 96 and 124 to methionines (see Methods). Crystals of the selenomethionine substituted double mutant FinO(26–186)L96,124M had the same unit cell dimensions as the wild type. Electrophoretic gel mobility shift analysis demonstrated that FinO(26–186)L96,124M binds FinP RNA with the same affinity as wild type FinO and FinO(26–186) (data not shown). A three-wavelength MAD data set was collected at beamline X12C at the National Synchrotron Light Source (NSLS). Solvent flattened, MAD phased electron density maps calculated to 2.6 Å resolu-

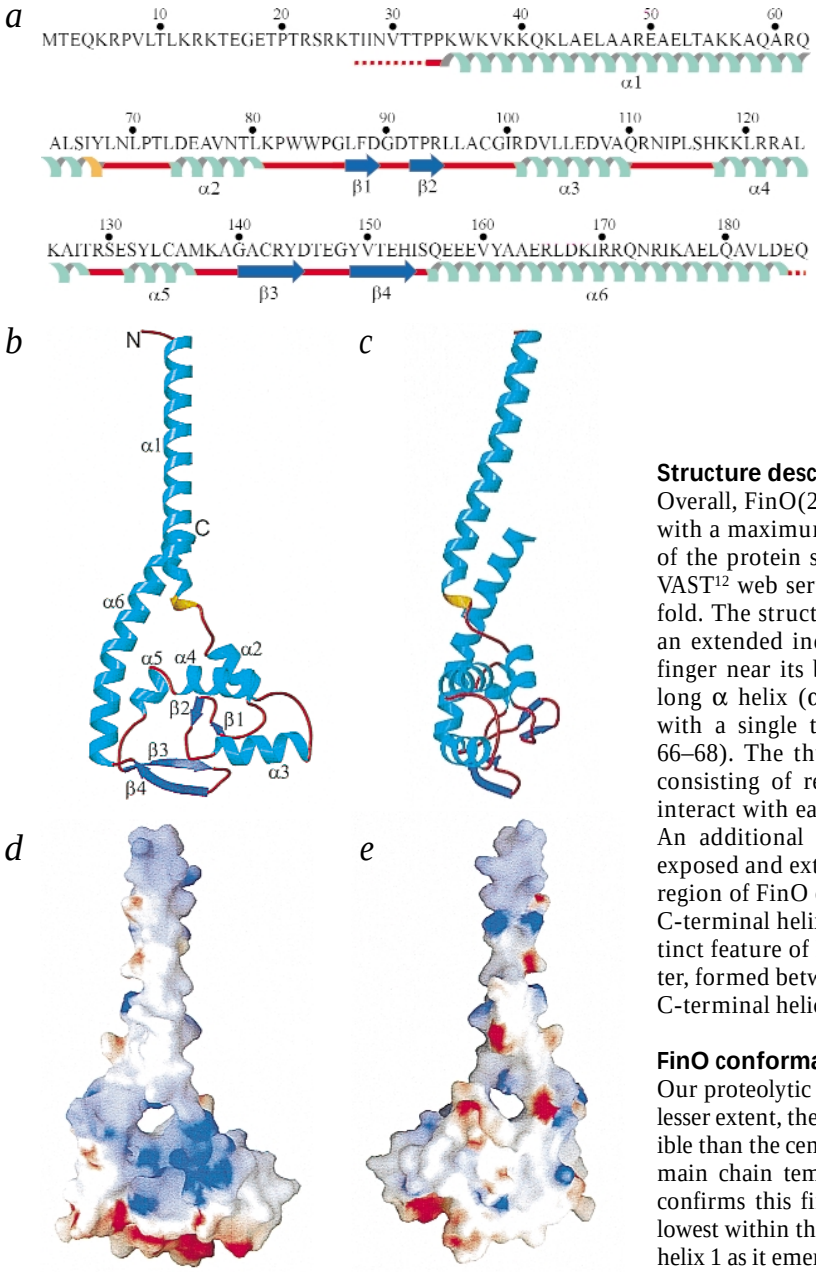

Fig. 2 Overall structure of FinO. ***a***, The primary sequence of FinO, with amino acids in the single letter amino acid code and the secondary structure elements labeled below the sequence. ***b***, Ribbon diagram of FinO, with the secondary structure motifs numbered as in (*a*) and the N-terminus and C-terminus labeled. ***c***, Ribbon diagram of FinO rotated 90° about a vertical axis with respect to (*b*). ***d***, Molecular surface representation of FinO, colored by electrostatic potential, with the protein in the same orientation as in (*b*). Increasing saturation of positive and negative potential is represented by blue and red, respectively. ***e***, Electrostatic potential surface of FinO, with the protein rotated 180° with respect to (*d*). The coloring scheme for the secondary structure motifs in (*a*), (*b*) and (*c*) are as follows: α-helices, cyan; β-strands, purple; regions of random coil, red; 3_{10}-helix, orange.

tion revealed excellent main and side chain density for residues 54–184 (Fig. 1*a*). Residues 33–53 adopted a solvent exposed helical conformation with generally poorer electron density than the rest of the molecule. Using this map, a model of FinO was built and partially refined. We subsequently collected diffraction data to 2.0 Å resolution from a crystal of the single point mutant, FinO(26–186)L124M. This data set was used in the final stages of refinement. Comparison of electron density maps calculated with the single and double mutant data indicate that the Leu to Met mutations have essentially no effect on the structure of FinO(26–186).

Our current model of FinO(26–186)L124M contains residues 33–184, and 212 water molecules. The model has been refined to an R-factor of 19.7% (R_{free} of 22.4%) using all data (20–2.0 Å) and has good stereochemistry (Table 1). A section of the $2F_o - F_c$ electron density map, phased with the final refined model, is shown in Fig. 1*b*.

Structure description

Overall, FinO(26–186) is a largely helical, elongated molecule with a maximum length of ~80 Å (Figs 2*b*,*c* and 3*a*). Searches of the protein structure data base using either the DALI[11] or VAST[12] web servers suggest that FinO adopts a novel protein fold. The structure is reminiscent of a right handed fist, with an extended index finger and thumb that touches the index finger near its base. The index finger corresponds to a 45 Å long α helix (α1) consisting of residues 33–65, which ends with a single turn of 3_{10}-helix at its C-terminus (residues 66–68). The thumb corresponds to a C-terminal helix (α6) consisting of residues 155–184. These two terminal helices interact with each other along a stretch of three helical turns. An additional 30 Å of the α1 helix is completely solvent exposed and extends past the C-terminus of FinO. The central region of FinO consists of five α-helices, including part of the C-terminal helix and two β-hairpins, β1-β2 and β3-β4. A distinct feature of FinO is the presence of a hole, ~5 Å in diameter, formed between the central region and the N-terminal and C-terminal helices.

FinO conformational flexibility

Our proteolytic mapping study[9] suggested that helix 1, and, to a lesser extent, the C-terminal 17 residues in helix 6, are more flexible than the central region (residues 62–174). An analysis of the main chain temperature factors (B-factors) throughout FinO confirms this finding (Fig. 3*b*). The main chain B-factors are lowest within the central region of FinO but rise dramatically in helix 1 as it emerges from the central region near residue 60, and near the C-terminus of helix 6 after residue 174.

FinO–RNA interactions

Studies have revealed that FinO contains two, separable, RNA binding regions, one encompassing residues 26–61 and the other consisting of residues 62–186 (ref. 9). Each region binds FinP specifically, albeit with 5- to 10-fold lower affinity than full length FinO or FinO(26–186). An electrostatic potential surface calculated for FinO(26–186) reveals positively charged regions that are likely to contact RNA directly (Fig. 2*d*,*e*). Residues near the N-terminus of helix 1 comprise one positively charged surface in the structure. A second large positively charged surface extends across one face of the central domain, and is composed of Lys and Arg residues from helices 4 and 6. Proteolytic mapping and direct RNA binding measurements of FinO deletion mutants have shown that these regions in helices 1 and 6 do contact RNA, although a direct role for helix 4 in RNA binding has yet to be established[9].

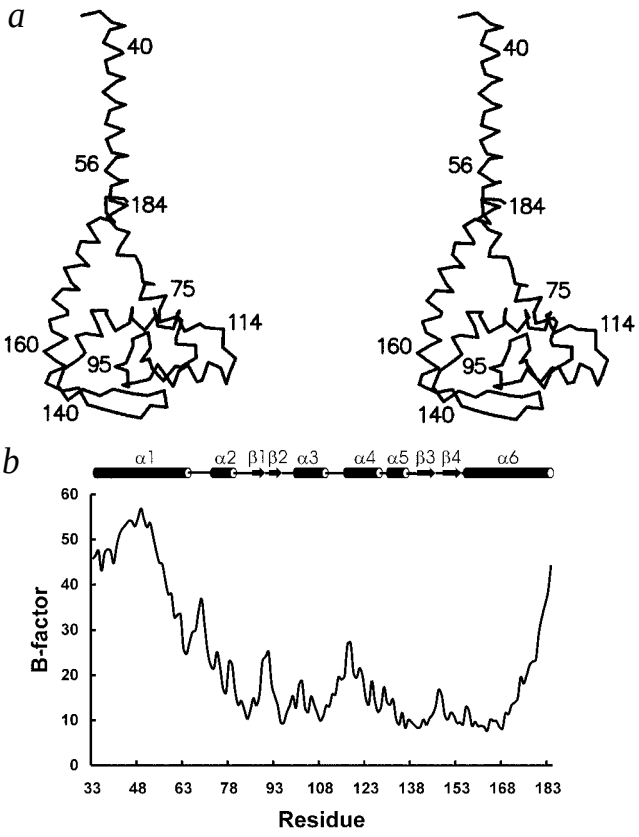

Fig. 3 Conformational flexibility in FinO. ***a***, Cα trace of FinO shown in stereo view. The position of approximately every 20th amino acid is indicated on the diagram. ***b***, Plot of the final refined B-factor values for the main chain Cα atoms of FinO. The secondary structure of FinO is indicated above the graph.

A quantitative analysis of the binding affinities of deletion mutants of FinP and *traJ* RNA has identified the 45 nucleotide SLII region of FinP as a minimal, high affinity binding site for FinO[13]. SLII consists of a 14 base pair stem, capped with a seven-residue loop, and flanked by 5′and 3′ single stranded tails of four and six nucleotides, respectively. Electrophoretic mobility shift assays have demonstrated that FinO binds this RNA as a monomer[9]. The C-terminal helix of FinO, important in RNA recognition *in vitro*, has also been shown to be important for protecting the nucleotides in the 5′ single stranded linker of FinP from RNase E degradation *in vivo*[10]. This suggests that the single stranded tails at the base of SLII interact with the positive face of the central domain of FinO (Fig. 4*a*). We predict that the SLII stem extends up from the central domain of FinO, along the positively charged N-terminal helix. Interestingly, the length of the N-terminal helix (45 Å) matches the predicted length of the SLII stem-loop. Positioned within the positively charged region near the N-terminus of helix 1 is an exposed tryptophan (Trp 36). It is tempting to speculate that this Trp might stack with unpaired residues in the loop. Similar stacking interactions have been observed between aromatic amino acid residues and unpaired bases in ribonucleoprotein (RNP)–RNA complexes and in a complex between a helical peptide derived from the λN transcriptional antiterminator and an RNA hairpin[14–16].

The electrostatic potential surface of FinO reveals a large negatively charged region, distinct from the proposed RNA binding surface (Fig. 2*d*,*e*). The negatively charged region, which is best viewed at the bottom of the molecule in Fig. 2*d*, is composed of residues from helix 3, the β3-β4 hairpin, and the N-terminal end of helix 6. Interestingly, the ColE1 Rop protein dimer, which is also involved in facilitating sense–antisense RNA interactions, also has separate positive and negatively charged surfaces[17,18]. Electrostatic repulsions between the negatively charged surfaces of these proteins and their respective RNAs might help to restrain the orientation of the RNA on the protein.

Our model assumes that the conformation of FinO does not change in response to RNA binding. We have shown, however, that helix 1 is flexible and is packed against the remainder of the protein through a modest contact with helix 6 that buries only 408 Å^2 of solvent accessible surface area. It is therefore possible that this helix could adopt a different orientation with respect to the rest of the protein in complex with RNA. A similar conformational adjustment in the C-terminal-most helix in the U1A RNP domain is observed upon interaction with RNA[15]. We are currently attempting to cocrystallize FinO bound to a minimal RNA substrate to directly determine the manner by which FinO contacts RNA.

FinP–*traJ* RNA association

Antisense–sense RNA recognition in natural bacterial systems is usually initiated by base pairing interactions between complementary loops in a 'kissing' complex[19]. Most of these loops (including those in FinP and *traJ* RNAs) contain a 5′-YUNR-3′ motif, first observed in the anticodon loops of tRNAs[20]. YUNR loops contain stacked bases in the 3′ portion of the loop that are pre-aligned for Watson-Crick interactions with a complementary single stranded RNA (as in codon–anticodon recognition) or with other loops. Mutations in the loop regions of FinP and *traJ* RNAs, but not in the stem or single stranded linker regions, cripple their ability to interact and effect repression. This strongly suggests that loop–loop interactions play an important part in FinOP mediated repression[21].

Our model of FinO in complex with FinP SLII suggests that FinO interacts with RNA to position the N-terminus of helix 1 near the unpaired loop (Fig. 4*a*). While the highest affinity binding site for FinO within FinP is SLII, FinO can also bind to a similar, complementary stem-loop structure in *traJ* RNA. Assuming that FinO interacts with both stem-loop structures in a similar way, we predict that the N-termini of the two FinO molecules bound to the complementary stem-loops will be in close proximity in a FinP–*traJ* RNA kissing complex (Fig. 4*b*).

Residues 1–25 of FinO do not play a role in binding individual RNA substrates[9], but it is possible that this positively charged region could specifically interact with, and stabilize, loop–loop interactions in a kissing complex. To test this prediction, we determined the relative abilities of FinO and FinO(26–186) to promote FinP–*traJ* RNA pairing in an *in vitro* duplexing assay (Fig. 4*c*,*d*; see Methods). While FinO dramatically enhances the rate of FinP–*traJ* RNA hybridization, we found that the enhancement is significantly less with FinO(26–186). The apparent rate constants for RNA hybridization, calculated from these and similar experiments, are: 5 (± 2) × 10^5 M^{-1} s^{-1} with no protein; 2.5 (± 1) × 10^7 M^{-1} s^{-1} with FinO; and 2.9 (± 1) × 10^6 M^{-1} s^{-1} with FinO(26–186). Thus, deletion of the N-terminal 25 amino acids of FinO reduces the rate of RNA association ~10-fold compared to the full length protein.

Conclusions

We have shown that N-terminal regions of FinO specifically enhance the rate of FinP–*traJ* RNA hybridization, perhaps through direct stabilization of a kissing RNA intermediate. Thus, FinO may

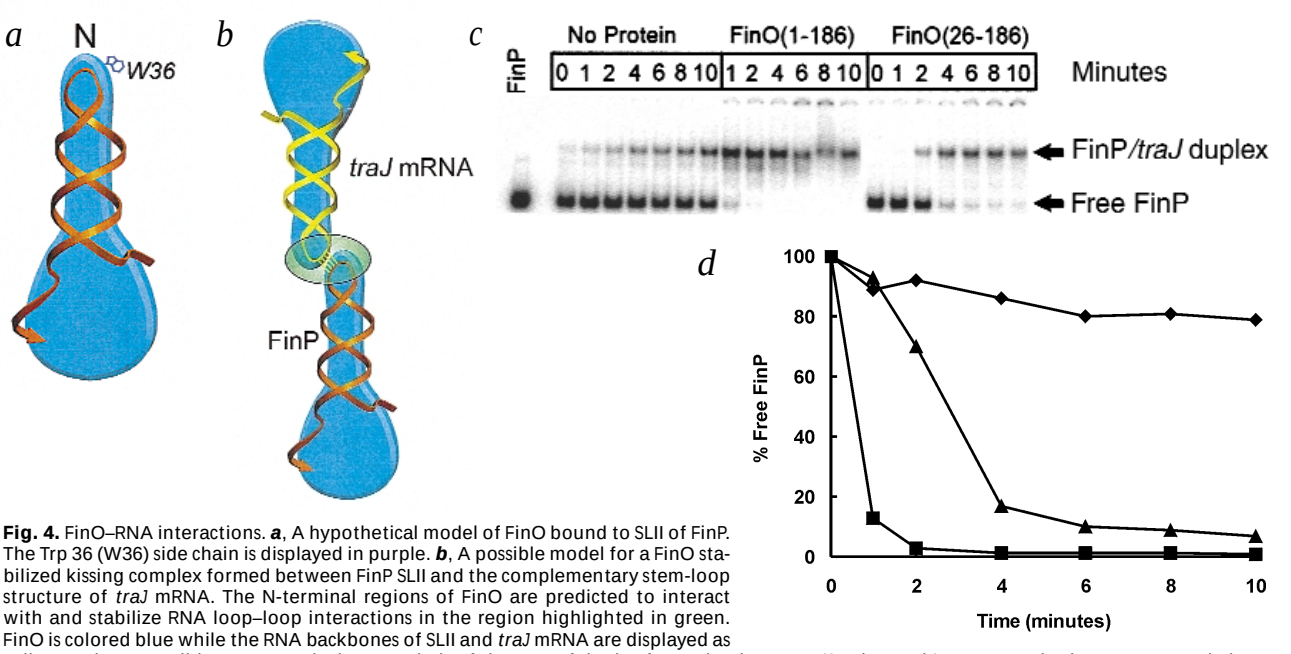

Fig. 4. FinO–RNA interactions. ***a***, A hypothetical model of FinO bound to SLII of FinP. The Trp 36 (W36) side chain is displayed in purple. ***b***, A possible model for a FinO stabilized kissing complex formed between FinP SLII and the complementary stem-loop structure of *traJ* mRNA. The N-terminal regions of FinO are predicted to interact with and stabilize RNA loop–loop interactions in the region highlighted in green. FinO is colored blue while the RNA backbones of SLII and *traJ* mRNA are displayed as yellow and orange ribbons, respectively. ***c***, Analysis of the rate of duplex formation between ^{32}P-FinP and ^{3}H-*traJ* RNA in the presence and absence of FinO(1–186) or FinO(26–186). In all cases, a 10-fold molar excess of *traJ* RNA was present in the duplex reaction. Duplex formation in the absence of protein was compared to duplex formation in the presence of 0.5 μM FinO(1–186) and 0.4 μM FinO(26–186). The amount of protein added was established by the amount of protein required to bind ~100% of 7.5 fmoles of FinP in a standard gel mobility shift assay. The rate of transfer of free FinP into the duplex with *traJ* RNA was used to calculate the apparent association rate constants. ***d***, The amount of free FinP RNA remaining at each time point during the duplexing assay shown in (*c*) is plotted for FinO(1–186) (squares), FinO(26–186) (triangles), and no FinO (diamonds).

act in a manner analogous to Rop, which stabilizes the association between the loops of RNAI and RNAII to regulate ColE1 plasmid replication[22]. FinO, however, adopts a structure that is unrelated to the compact, four-helix bundle structure of the Rop dimer[18]. The highly extended structure of FinO is probably necessary to allow this relatively small protein to contact the interacting loops in the kissing complex, as well as single stranded regions in FinP that are otherwise highly susceptible to RNase degradation.

Methods

Expression and purification. The expression and purification of FinO(26–186), FinO(26–186)L124M and FinO(26–186)L96,124M follows the described protocol[9]. Selenomethionine substituted FinO(26–186)L96,124M was expressed by incorporation of selenomethionine into the bacterial growth media, under growth conditions that repress methionine biosynthesis[23].

Mutagenesis. Site directed mutagenesis by overlap extension[24] was used to construct *finO(26–186)L124M* and *finO(26–186)L96, 124M*. The codon encoding Leu 124 was first mutated to methionine. Sequencing was used to verify the introduction of this mutation. A subsequent round of overlap extension was used to construct *finO(26–186)L96,124M*. The FinO mutants were cloned back into the pGEX-KG vector (Amersham-Pharmacia Biotech), in frame and downstream of the glutathione-S-transferase gene. The sequence of the oligonucleotide primer pairs used for introducing the point mutations into *FinO(26–186)* are 5′-GACACGCCCCGGCTTATGGCCTGCGGT-3′ and 5′-ACCGCAGGCCATAAGCCGGGGCGTGTC-3′ for the L96M substitution and 5′-GCGCAGGGCGATGAAGGCCATC-3′ and 5′-GATGGCCTTCATCGCCCTGCGC-3′ for the L124M substitution.

Crystallization. All crystals were grown at 4 ºC by the hanging drop, vapour diffusion method. For the hanging drop, 1 μL of a 10 mg mL^{-1} protein solution in 150 mM NaCl, 50 mM 2-(4-morpholino)-ethane sulfonic acid (pH 6.5), 0.1% β-mercaptoethanol (v/v) and 1 mM EDTA was mixed with 1 μL of reservoir solution (12% PEG 4000 and 50 mM Tris, pH 7.2). Crystals of FinO(26–186) grew as thin plates to a maximum size of 400 μm × 200 μm × ~5 μm within seven hours. Crystals of FinO(26–186)L124M and selenomethionine substituted FinO(26–186)L96,124M were nucleated with reservoir solution containing crushed FinO(26–186) crystals. The maximum size of these seeded crystals was approximately the same as for FinO(26–186).

Data collection and processing. Crystals were harvested in reservoir solution and transferred to a series of reservoir solutions with increasing glycerol concentrations to a maximum concentration of 25% (v/v). These crystals were then flash frozen directly in a 100 K N_2 stream for data collection. The MAD data set was collected with a Brandeis 1K CCD detector at beamline X12C at the NSLS. Data from FinO(26–186)L124M crystals were collected at beamline 14-BM-D at the Advanced Photon Source (APS) using a ADSC Quantum-4 CCD detector. All data were indexed and scaled using Denzo and Scalepack[25]. The selenomethionine positions and initial MAD phases were calculated using the program SOLVE, treating the data as a special case of multiple isomorphous replacement with anomolous scattering, and using the inflection wavelength data as a pseudo-native data set[26]. Phases were further improved by solvent flattening and histogram matching as implemented in the program DM[27]. The solvent mask was edited to include the solvent exposed helix 1.

Model building and refinement. The MAD phased, solvent flattened electron density map calculated to 2.6 Å resolution gave excellent electron density for the region corresponding to residues 54–184 and poorer but interpretable density for the region corresponding to residues 38–53. Using this map, we built a model incorporating most of the side chains for residues 38–183, using the programs O[28] and Xtalview/Xfit[28,29]. In the early stages of refinement we used the program X-PLOR[30] for restrained individual B-factor refinement, positional refinement and simulated annealing protocols. After three rounds of refinement, the R-factor was brought down to 32.7 % (R_{free} 37.3%). Residues 34–37 and 184 were

Table 1 X-ray data collection, phasing and refinement statistics

	High resolution FinO(26–186)L124M	MAD data collection Se-FinO(26–186)L96,124M		
Data set		λ1	λ2	λ3
Wavelength (Å)	0.9574	0.9790	0.9786	0.9640
Resolution (Å)	20–2.0	20–2.6	20–2.6	20–2.6
Observations	109,290	58,397	58,355	58,307
Unique reflections	14,726	6,841	6,839	6,832
Data coverage total / final shell (%)[1]	97.3 / 87.0	97.2 / 97.7	97.2 / 97.8	97.2 / 98.3
R_{merge} total/final shell (%)[2]	4.7 / 11.0	6.1 / 10.7	6.6 / 11.4	6.2 / 11.4
Phasing (20.0–2.0 A)				
Overall figure of merit	0.65 (SOLVE; ref. 26)			

Refinement statistics (20–2.0 Å)			
R_{cryst}[3] total / final shell (%)	19.7 / 20.4	Average B-factor (Å^2)	24.1
R_{free}[4] total / final shell (%)	22.4 / 23.4	Number of atoms	
R.m.s. deviations		Protein	1,219
Bond lengths (Å)	0.009	Water	212
Bond angle (°)	1.35	Ramachandran analysis[5]	
		Most favored	96.4%
		Additionally allowed	3.6%

[1]The highest resolution shell for FinO(26–186)L124M was 2.05–2.00 Å and for Se-FinO(26–186)L96,124M it was 2.69–2.60 Å.
[2]$R_{merge} = \Sigma|<I> - I| / \Sigma<I>$.
[3]$R_{cryst} = \Sigma||F_o| - |F_c|| / \Sigma|F_o|$.
[4]R_{free} calculated with 10% of all reflections excluded from refinement stages using high resolution data.
[5]Ramachandran analysis was performed with the program Procheck[36].

now introduced into our model and refinement was continued using the maximum likelihood torsion angle dynamics algorithm from the CNS package, employing a solvent mask and an overall anisotropic B-factor correction[31]. At an R-factor of 30% (R_{free} 34.7%), additional refinement was continued with the 2.0 Å data set collected from the FinO(26–186)L124M crystals. The final working R-factor was 19.7% (R_{free} 22.4%). Figures were prepared with the programs BOBSCRIPT[32], MOLSCRIPT[33], RASTER3D[32,34] and GRASP[35].

FinP–*traJ* RNA duplexing assay. FinP–*traJ* RNA duplex analyses were performed as described[10] with minor changes. Briefly, 0.15 nM ^{32}P-FinP and ^{3}H-*traJ*184 RNA in 10-fold molar excess were incubated in 50 μL of duplexing buffer (25 mM Tris-HCl, pH 8.0, 4 mM magnesium acetate, 0.4 mM EDTA, 40 mM NaCl, 40 μg mL^{-1} RNase-free bovine serum albumin, 0.3 units mL^{-1} RNasin) in the presence or absence of various FinO deletion derivatives. In some cases, a two-fold or five-fold molar excess of *traJ*184 RNA was used in order to produce measurable rates of duplex formation. Aliquots (5 μL) were removed at specified time points and added to 10 μL ice-cold stop solution (95% formamide, 10 mM EDTA, 0.5% each xylene cyanol and bromophenol blue) and electrophoresed on 8% native polyacrylamide gels. Apparent kinetic rate constants for FinP–*traJ* RNA association in the absence or presence of FinO(1–186) or FinO(26–186) were calculated from multiple experiments as described[10].

Coordinates. The atomic coordinates have been deposited with the Protein Data Bank (accession code 1DVO).

Acknowledgments
We wish to thank S. Williams, R. Sweet and the staff of beamline X12C (NSLS), and W. Schildkamp and the staff of beamline 14-BM-D (APS) for excellent technical support during crystallographic data collection. We also wish to thank M. James for encouragement and insightful comments. This work was supported by grants from the Alberta Heritage Foundation for Medical Research and the Medical Research Council of Canada (to J.N.M.G.).

Correspondence should be addressed to J.N.M.G. *email: mark.glover@ualberta.ca*

Received 31 January, 2000; accepted 25 May, 2000.

1. Frost, L.S., Ippen-Ihler, K. & Skurray, R.A. *Microbiol. Rev.* **58**, 162–210 (1994).
2. Finnegan, D. & Willetts, N. *Mol. Gen. Genet.* **119**, 57–66 (1972).
3. Mullineaux, P. & Willetts, N. *Basic Life. Sci.* **30**, 605–614 (1985).
4. van Biesen, T. & Frost, L.S. *Mol. Microbiol.* **14**, 427–436 (1994).
5. Jerome, L.J., van Biesen, T. & Frost, L.S. *J. Mol. Biol.* **285**, 1457–1473 (1999).
6. Lee, S.H., Frost, L.S. & Paranchych, W. *Mol. Gen. Genet.* **235**, 131–139 (1992).
7. van Biesen, T., Soderbom, F., Wagner, E.G. & Frost, L.S. *Mol. Microbiol.* **10**, 35–43 (1993).
8. Koraimann, G., Teferle, K., Markolin, G., Woger, W. & Hogenauer, G. *Mol. Microbiol.* **21**, 811–821 (1996).
9. Ghetu, A.F., Gubbins, M.J., Oikawa, K., Kay, C.M., Frost, L.S. & Glover, J.N.M. *Biochemistry* **38**, 14036–14044 (1999).
10. Sandercock, J.R. & Frost, L.S. *Mol. Gen. Genet.* **259**, 622–629 (1998).
11. Holm, L. & Sander, C. *J. Mol. Biol.* **233**, 123–138 (1993).
12. Madej, T., Gibrat, J.F. & Bryant, S.H. *Proteins* **23**, 356–369 (1995).
13. Jerome, L.J. & Frost, L.S. *J. Biol. Chem.* **274**, 10356–10362 (1999).
14. Price, S.R., Evans, P.R. & Nagai, K. *Nature* **394**, 645–650 (1998).
15. Oubridge, C., Ito, N., Evans, P.R., Teo, C.H. & Nagai, K. *Nature* **372**, 432–438 (1994).
16. Legault, P., Li, J., Mogridge, J., Kay, L.E. & Greenblatt, J. *Cell* **93**, 289–299 (1998).
17. Predki, P.F., Nayak, L.M., Gottlieb, M.B. & Regan, L. *Cell* **80**, 41–50 (1995).
18. Banner, D.W., Kokkinidis, M. & Tsernoglou, D. *J. Mol. Biol.* **196**, 657–675 (1987).
19. Wagner, E.G. & Simons, R.W. *Annu. Rev. Microbiol.* **48**, 713–742 (1994).
20. Franch, T., Petersen, M., Wagner, E.G., Jacobsen, J.P. & Gerdes, K. *J. Mol. Biol.* **294**, 1115–1125 (1999).
21. Koraimann, G., Koraimann, C., Koronakis, V., Schlager, S. & Hogenauer, G. *Mol. Microbiol.* **5**, 77–87 (1991).
22. Eguchi, Y. & Tomizawa, J. *J. Mol. Biol.* **220**, 831–842 (1991).
23. Doublié, S. *Methods Enzymol.* **276**, 523–530 (1997).
24. Ho, S.N., Hunt, H.D., Horton, R.M., Pullen, J.K. & Pease, L.R. *Gene* **77**, 51–59 (1989).
25. Otwinowski, Z. & Minor, W. *Methods Enzymol.* **276**, 307–326 (1997).
26. Terwilliger, T.C.D. *Acta Crystallogr. A* **43**, 1–5 (1987).
27. Cowtan, K. Joint CCP4 and ESF-EACBM newsletter on protein crystallography **31**, 24–28 (1994).
28. Jones, T.A., Zhou, J.Y., Cowan, S.W. & Kjeldgaard, M. *Acta Crystallogr. A* **47**, 110–119 (1991).
29. McRee, D.E. *J. Struct. Biol.* **125**, 156–165 (1999).
30. Brünger, A.T. *X-PLOR: a system for X-ray crystallography and NMR.* (Yale University Press, New Haven, Connecticut; 1992).
31. Brunger, A.T. *et al. Acta Crystallogr. D* **54**, 905–921 (1999).
32. Esnouf, R.M. *J. Mol. Graph. Model.* **15**, 133–138 (1997).
33. Kraulis, P.J. *J. Appl. Crystallogr.* **24**, 946–950 (1991).
34. Merritt, E.A. & Bacon, D.J. *Methods Enyzmol.* **277**, 505–524 (1997).
35. Nicholls, A., Sharp, K.A. & Honig, B. *Proteins* **11**, 281–296 (1991).
36. Laskowski, R.A., MacArthur, M.W., Moss, D.S. & Thornton, J.M. *J. Appl. Crystallogr.* **26**, 283–291 (1993)